

Poisson Solver for Upscaling the Physical Properties of Porous Materials

Tatyana Khachkova and Vadim Lisitsa(✉)

Sobolev Institute of Mathematics SB RAS, 4 Koptug ave, Novosibirsk 630090, Russia
lisitsavv@ipgg.sbras.ru

Abstract. In this paper, we present an iterative solver for Poisson equation. The approach is essentially oriented on upscaling the physical parameters of porous materials, such as electrical resistivity, thermal conductivity, pressure field computation. The algorithm allows solving Poisson equation for strongly heterogeneous media with small-scale high-contrast heterogeneities. The solver is based on the Krylov-type iterative method with a pseudo-spectral preconditionner, thus the convergence rate is independent on the sample size, but sensitive to the contrast of physical properties in the model. GPU-based implementation of the algorithm allows performing simulations for the samples of the size 400^3 using a single GPU.

Keywords: Pore scale · Poisson equation · GP-GPU · Numerical upscaling

1 Introduction

Numerical upscaling the physical properties of porous materials is a rapidly developing area of research, due to availability of micro-tomographic images of porous materials and computational resources. In particular, digital rock physics is getting a common tool in petrophysical analysis of rocks [4] to estimate absolute permeability [5,11], relative permeability for two- and three-phase flows [3], diffusion of chemicals for reactive transport [20,21], thermal conductivity [10], electrical resistivity [5,28]. To evaluate the effective properties of porous material one needs to simulate a specific physical process at the pore scale and then use averaging of the solution over the entire sample. The first step is the most computationally intensive and requires the numerical solution of partial differential equations. In particular, fluid flow simulation is based on the solution of Navier-Stokes or steady-state Stokes equations, where solving the Poisson equation is the principal step especially if the projection-type methods are used [8]. Numerical estimation of electrical resistivity and thermal conductivity is essentially based on the solution of Poisson equation [10,28]. Nowadays, digital rock physics laboratories are well equipped with micro-tomographic scanners but

The research was supported by the Russian Science foundation grant no. 21-71-20003.

© Springer Nature Switzerland AG 2021
O. Gervasi et al. (Eds.): ICCSA 2021, LNCS 12949, pp. 532–545, 2021.
https://doi.org/10.1007/978-3-030-86653-2_39

have limited access to high performance computing facilities. Thus, an appropriate option is to use GP-GPU servers for numerical simulations in digital rock physics applications.

We present the numerical algorithm for solving Poisson equation in strongly heterogeneous media oriented on the use of graphic processor units. Strongly inhomogeneous media includes small-scale heterogeneities [6] and high amplitudes of the inhomogeneities. There are several approaches to solve the Poisson equation, but the most commonly used are the Krylov-type methods with appropriate preconditioners. Incomplete LU factorization [14], including low-rank approximations [9,17] and multi-grid [16,25] are commonly used to precondition a discretized Poisson equation. First class approaches require storing the matrix and its factors. Approaches from a different class require problems solving in a series of nested grids and solutions storage. However, if we consider strongly heterogeneous geomaterials models, a scale coarsening changes the topology and geometry of pore space, that is the main conductive model part. Thus, the problem on a coarse grid will not be closer to the true one than the problem for homogeneous media. At the same time, the spectral method [7] using GPUs can be effectively applied to solve the Poisson equation with constant conductivity.

The paper is structured as follows. We formulate the problem in Sect. 2. Finite-difference approximation is provided in Sect. 3. Description of the solver and the preconditioner are presented in Sect. 4. Numerical experiments are introduced in Sect. 5.

2 Numerical Estimation of Electrical Resistivity

The goal of this research is to simulate the electric current in rock samples using the 3D microtomographic images. Thus, two problems should be solved. First, we need to calculate the electric current in the inhomogeneous model for a given potentials difference applied to the opposite sample sides. Second, it's necessary to restore the scalar (tensor) electrical resistivity at which the resulting electric current was equal to that in the original model for a given potentials difference.

Consider the domain $\Omega = [0, X_1] \times [0, X_2] \times [0, X_3]$ with inhomogeneous media and the Poisson equation:

$$\nabla \cdot (\sigma(\boldsymbol{x}) \nabla \varphi(\boldsymbol{x})) = 0, \tag{1}$$

where $\sigma = \sigma(\boldsymbol{x})$ is the electrical conductivity, $\varphi = \varphi(\boldsymbol{x})$ is the scalar electric potential. We assume that there are no charges inside the computational domain, so the right-hand sides are equal to zero. The Dirichlet boundary conditions are used at two opposite sides $x_1 = 0$ and $x_1 = X_1$, that is

$$\varphi(\boldsymbol{x})|_{x_1=0} = \Phi_0, \, \varphi(\boldsymbol{x})|_{x_1=X_1} = \Phi_1, \tag{2}$$

where Φ_0 and Φ_1 are the potentials. On the other sides of the domain, we apply Neumann boundary conditions

$$\begin{aligned} \nabla\varphi \cdot \boldsymbol{n}|_{x_2=0} = 0, \, \nabla\varphi \cdot \boldsymbol{n}|_{x_2=X_2} = 0, \\ \nabla\varphi \cdot \boldsymbol{n}|_{x_3=0} = 0, \, \nabla\varphi \cdot \boldsymbol{n}|_{x_3=X_3} = 0. \end{aligned} \tag{3}$$

Neumann boundary conditions are used to simulate laboratory experiments in which a sample is placed in insulator ports.

The spatial distribution of the electric potential $\varphi(\boldsymbol{x})$ is the solution of Eq. (1), after that the electric current can be defined as

$$J_1 = \int_0^{X_2} \int_0^{X_3} \sigma(\boldsymbol{x}) \frac{\partial \varphi}{\partial x_1} dx_2 dx_3. \tag{4}$$

Note, that the current should be independent of spatial coordinates.

On the contrast, if homogeneous media with unknown conductivity $\hat{\sigma}$ is considered, Eq. (1) turns into

$$\nabla \cdot (\hat{\sigma} \nabla \hat{\varphi}(\boldsymbol{x})) = 0, \tag{5}$$

with boundary conditions (2) and (3). Solution of the this equation can be constructed analytically:

$$\varphi(\boldsymbol{x}) = \Phi_0 + \frac{\Phi_1 - \Phi_0}{X_1} x_1. \tag{6}$$

In addition, electric current in the direction x_1 satisfies the Ohm's law:

$$\hat{J}_x = \int_0^{X_2} \int_0^{X_3} \sigma(\boldsymbol{x}) \frac{\partial \varphi}{\partial x_1} dx_2 dx_3 = \hat{\sigma} \frac{\Phi_1 - \Phi_0}{X_1} S_1, \tag{7}$$

where S_1 is the surface area of the sample cross-section normal to the direction x_1.

Assuming that a given potentials difference at two opposite sides of the sample causes the same electric current either in an inhomogeneous or in a homogeneous media, that is $\hat{J}_x = J_x$, the electrical conductivity of the effective material can be reconstructed:

$$\hat{\sigma} = J_x \frac{X_1}{S_1} \frac{1}{\Phi_1 - \Phi_0}. \tag{8}$$

The most laborious computational problem in the numerical estimation of electrical resistivity or conductivity is the solution of the Poisson equation in strongly heterogeneous media, where the characteristic size of inhomogeneities is form one to ten voxels, and the conductivity amplitude varies by several orders of magnitude.

3 Finite-Difference Approximation

We propose to use a finite volume of conservative finite-difference method to approximate the Eq. (1) in an inhomogeneous domain. Let's introduce a grid with steps h_1, h_2, and h_3 in the directions x_1, x_2, and x_3 respectively, so that $(x_j)_{m_j} = h_j m_j$. Also, we introduce grid cells

$$C_{m_1,m_2,m_3} = \prod_{j=1}^{3} [h_j(m_j - 1/2), h_j(m_j + 1/2)],$$

where $\prod$ denotes the direct product of sets. Let's define that the potential and conductivity are constant within the grid cell, while they can be discontinuous across the cell faces. After that, the finite-difference approximation of the Poisson equation (1) can be introduced as:

$$\begin{aligned}
&\frac{1}{h_1}\left(\tilde{\sigma}_{m_1+1/2,m_2,m_3} D_1[\varphi]_{m_1+1/2,m_2,m_3} - \tilde{\sigma}_{m_1-1/2,m_2,m_3} D_1[\varphi]_{m_1-1/2,m_2,m_3}\right) \\
&+\frac{1}{h_2}\left(\tilde{\sigma}_{m_1,m_2+1/2,m_3} D_2[\varphi]_{m_1,m_2+1/2,m_3} - \tilde{\sigma}_{m_1,m_2-1/2,m_3} D_2[\varphi]_{m_1,m_2-1/2,m_3}\right) \\
&+\frac{1}{h_3}\left(\tilde{\sigma}_{m_1,m_2,m_3+1/2} D_3[\varphi]_{m_1,m_2,m_3+1/2} - \tilde{\sigma}_{m_1,m_2,m_3-1/2} D_3[\varphi]_{m_1,m_2,m_3+1/2}\right) = 0,
\end{aligned} \tag{9}$$

where the finite-difference operators are defined as

$$\begin{aligned}
D_1[\varphi]_{m_1+1/2,m_2,m_3} &= \frac{\varphi_{m_1+1,m_2,m_3} - \varphi_{m_1,m_2,m_3}}{h_1}, \\
D_2[\varphi]_{m_1,m_2+1/2,m_3} &= \frac{\varphi_{m_1,m_2+1,m_3} - \varphi_{m_1,m_2,m_3}}{h_2}, \\
D_3[\varphi]_{m_1,m_2,m_3+1/2} &= \frac{\varphi_{m_1,m_2,m_3+1} - \varphi_{m_1,m_2,m_3}}{h_3},
\end{aligned} \tag{10}$$

and the electrical conductivity at the faces of grid cells is calculated as an harmonic averaging of those from the joint cells:

$$\begin{aligned}
\frac{1}{\tilde{\sigma}_{m_1+1/2,m_2,m_3}} &= 2\left(\frac{1}{\sigma_{m_1+1,m_2,m_3}} + \frac{1}{\sigma_{m_1,m_2,m_3}}\right), \\
\frac{1}{\tilde{\sigma}_{m_1,m_2+1/2,m_3}} &= 2\left(\frac{1}{\sigma_{m_1,m_2+1,m_3}} + \frac{1}{\sigma_{m_1,m_2,m_3}}\right), \\
\frac{1}{\tilde{\sigma}_{m_1,m_2,m_3+1/2}} &= 2\left(\frac{1}{\sigma_{m_1,m_2,m_3+1}} + \frac{1}{\sigma_{m_1,m_2,m_3}}\right).
\end{aligned} \tag{11}$$

A detailed description of constructing the approximation can be found, for example, in [10,13,14,27]. This modification of the coefficients, preserving the second order of convergence of the finite-difference solution, is represented in [10,19,24,26].

4 Iterative Solver

The Krylov-type methods are usually used to solve a system of linear algebraic equations. However, the condition number of the system is high because the spectrum of the matrix tends to expand to the entire real axis with increasing matrix size to approximate the differential operator. In addition, in geomaterials, electrical conductivity (resistivity) can vary by several orders, while increasing the condition number. To improve convergence several possible preconditioners are used. Among them, the incomplete LU factorization [14,18], including low-rank approximations [9,17] and the multi-grid [16,25] are commonly used. The first class approaches require storing the matrix and its factors; thus, at least $4N$ of additional variables must be stored in memory, where N is the size of the

problem (the number of grid points in the computational domain). Approaches from another class require to solve a set of problems (1) at a series of nested grids storing the solutions. However, if we consider strongly heterogeneous models changing the scale or a grid size changes the topology and geometry of the pore space, that is the main conductive model part. Thus, the problem on a coarse grid will not be closer to the true one than that for the homogeneous media. At the same time, the system of equations (9) with constant conductivity is efficiently solved by spectral method [7,22] using GPUs.

Let's consider system of equations (9) written in a short form:

$$L\varphi = f.$$

After preconditioning, we can get a system

$$(L_0^{-1}L)\varphi = A\varphi = L_0^{-1}f,$$

where L and L_0 are approximations of the Laplace operator for inhomogeneous and homogeneous media, respectively. The most time consuming part of the algorithm is the calculating the matrix-vector multiplication. The action of the matrix L is described by the formulas (9), while the action of L_0^{-1} requires to solve a system of equations (9) with constant conductivity for different right-hand sides. To calculate $L_0^{-1}\psi$ for an arbitrary ψ we propose to use spectral methods. Applying the Fourier transform with respect to x_2 and x_3 to the Eq. (1), we get a series of one-dimensional problems:

$$\frac{d^2\Phi}{dx_1^2} - (k_2^2 + k_3^2)\Phi = \hat{g}(x_1, k_2, k_3)/\sigma_0, \tag{12}$$

where Φ is the Fourier image of the unknown function, and $\hat{g}(x_1, k_2, k_3)$ is the image of the right-hand side. It's necessary to note, that the problem can be solved independently for each frequency. To solve one-dimensional equations, the same approximation is used as in Eq. (9), after that the Thomas algorithm for three-diagonal matrices is applied. And then we apply the inverse Fourier transform to the solution. So, the solution of the problem can be represented as:

$$\varphi_0(\boldsymbol{x}) = \frac{1}{\sigma_0}\mathcal{F}_{2,3}^{-1}\left[\hat{L}(k_2, k_3)^{-1}\mathcal{F}_{2,3}[f(\boldsymbol{x})]\right],$$

where $\mathcal{F}_{2,3}$ is the Fourier transform operator, $\hat{L}(k_2, k_3)$ is the 1D operator, that depends on the spatial frequencies k_2 and k_3. Parameter σ_0 is equal to fluid conductivity.

4.1 GPU-Based Implementation

The algorithm is implemented using GP-GPU computations, so that all main steps of the algorithm are executed using GPU with minimal data flows between the device and the host. At the preliminary step we read the model, preprocess it, allocate the memory to store solution and the auxiliary variables to

BCGStab and for the preconditionner. After that, all the actual computations are performed by GPU only. It includes, application of qFFT along x_2 and x_3 directions, solution of the series of 1D problems, and updating BCGStab vectors. Only after the convergence of the algorithm, the solution is transferred to the RAM.

We estimate the amount of memory needed for computations. In the RAM, we need to store the model and the solution, which have the size of $N_1N_2N_3$, where N_j is the number of grid points in corresponding direction x_j. For this algorithm no more RAM is allocated. Implementation of the BCGStab on the GPU requires memory to store a model, a solution, and right-hand sides, i.e., three main arrays of the same size. Moreover, the standard implementation of BICGStab still requires an additional five arrays of the specified size $N_1N_2N_3$ [23]. Next, we additionally store the FFT image of vector $\hat{g}(x_1, k_2, k_3)$, that is complex array of the size $N_1N_2N_3$, to implement the FFT-based preconditioner. Finally, the implementation of Thomas algorithm requires additional storage of the same size array. Indeed, the solution of one-dimensional problems is implemented independently for each spatial frequency $k_2^2 + k_3^2$, so that one GPU thread solves a problem only for one frequency. Please note that we solve one-dimensional problems for homogeneous media. Thus, the matrix can be described by only one parameter - the square of the spatial frequency divided by the square of the spatial step. Thomas algorithm requires a storage of matrix factors. Therefore, we need to store an array of size N_1. Moreover, such an array is required by every GPU thread, so we decided to pre-allocate memory for it; i.e., we store N_2N_3 arrays of N_1 size just for the parallel Thomas algorithm implementation.

Finally, we need $11N_1N_2N_3 * 8$ bytes to store all the variables on GPU in case of double-precision computations. A simple estimate shows that for numerical experiments, a 400^3 sample requires 5 Gb of memory, while a 500^3 sample requires almost 11 Gb of GPU memory.

5 Numerical Experiments

5.1 Verification of the Algorithm

Parallel Resistors. To verify the developed algorithm, we calculated the electric current for sets of simple models. First of all, a sample was considered with one conducting channel, the cross-section of which is square with a side equal to one-fifth of the sample side. At that, the sample was cubical. The electrical conductivities were for the background $\sigma_b = 0.5S$ and for the channel $\sigma_c = 5S$, the grid step was equal to 1 μm. The size of samples was varied as $5 \cdot 2^n$ points, where $n = 0, ..., 6$, i.e. from 5 to 320 points. We calculated the electric potential inside the sample and estimated the effective electrical conductivity using the formula (8). On the other hand, the model under consideration is equivalent to an electrical contour with parallel resistors, therefore, according to Ohm's law, the effective conductivity is

$$\sigma_{||} = \sigma_b S_b/S + \sigma_c S_c/S,$$

where S_b and S_c are the background and channel areas, while S is the cross-section area of the sample. For described experiments $\sigma_{||}$ was 0.68 S and for all considered computational domain sizes the estimated conductivity was $0,68$ S up to machine precision. Note, that one BiCGStab iteration was required for the algorithm to converge.

Serial Resistors. The second series of experiments was carried out for layered media with layers normal to the primary direction of the potential change. This type of models is a serial resistors, and the effective conductivity can be estimated as

$$\frac{1}{\sigma_\perp} = \frac{l_b}{L}\frac{1}{\sigma_b} + \frac{l_c}{L}\frac{1}{\sigma_c},$$

where l_b is the total background thickness, and l_c is the total layers' thickness, and L is the length of the sample. We considered $\sigma_c = 5$ S, and $\sigma_b = 0.5$ S/m to provide the electric current. We changed the size of the models in the same way as before. In addition to the size of the model, we changed the model itself in two ways. First, we kept one conductive layer and increased its thickness proportional to the domain size. Second, we kept the layer thickness but increased the number of layers proportional to the size of the domain. Regardless of the size of the models, BiCGStab converged in 3 iterations with a relative residual not exceeding 10^{-13}. The numerical estimates of electrical conductivity converged to a theoretical estimate with the first order.

5.2 Performance Analysis

Dependence on the Model Size. In this section, we present experiments measuring the performance of the algorithm, depending on the samples size, contrast in the conductivity and the typical size of the heterogeneities.

We varied the domain size as $N_j \in [20, 40, 80, 160, 320]$ points. Note, that the algorithm works differently in the direction x_1 and in the directions x_2 and x_3. Thus, it is necessary to consider cases, where N_1 is fixed, while N_2 and N_3 are changed, but $N_2 = N_3$, and the opposite case, when N_1 is changed, but $N_2 = N_3$ are fixed. Thus, 25 model size combinations were considered. To create the model, a random sample was generated with the size of one homogeneous cell, equals to 4^3 voxels. A random number generator was used to fill the cells with conductivities $\sigma = 10^{R([-3,1])}$, where $R([-3,1])$ is the homogeneous distribution within the interval $[-3,1]$. To obtain stable estimates of the iterations number and the computation time, it were performed a series of 10 simulations for various statistical model realizations. We measured the number of iterations, required for convergence (Fig. 1) and time per iteration (Fig. 2). The number of iterations needed for the convergence depends on the number of grid points along x_1 direction (along the main current), but does not depend on the other two sizes of the sample. As for the time per a single iteration, it increases linearly with the size of the model in x_1 direction, since the Thomas algorithm has a linear computational complexity with respect to the size of the problem. Further, the

iteration time increases quadratically with simultaneous increasing sizes along x_2 and x_3 direction, which is also reconfirmed by theoretical estimates of the FFT computational complexity.

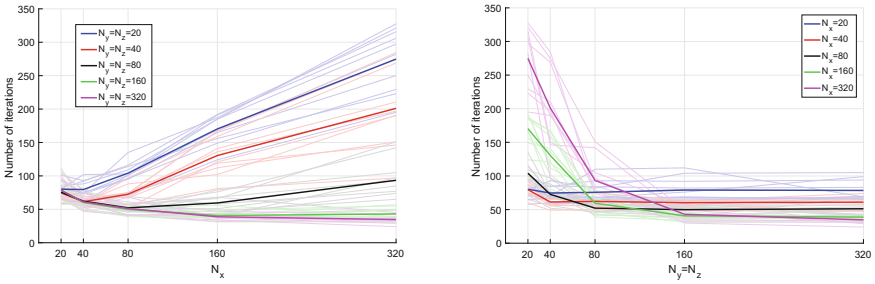

Fig. 1. Dependence of the number of iterations for convergence on the grid points number in the x_1 direction (left) and on different sizes of the model along the FFT directions (right). The thick lines correspond to the means for the statistical realizations of models, and the thin lines correspond to the separate realizations.

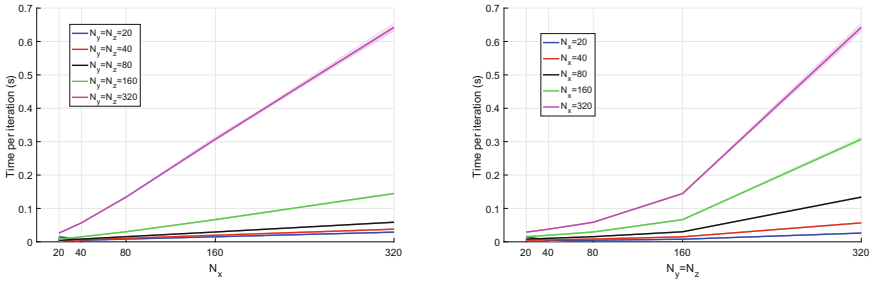

Fig. 2. Dependence of the time per iteration on the grid points number in x_1 direction (left) and on the model size along the FFT directions (right). The thick lines correspond to the means for the statistical realizations of models.

Dependence on the Resistivity Contrast. We applied the algorithm to the Bentheimer sandstone samples described in [6]. It were considered the images with a resolution of 5.58 μm and 3.44 μm per voxel, which are images B and C from [6], respectively. The size of the samples was 400^3 voxels. These two models were used to investigate the effect of the conductivity contrast on the number of iterations required for convergence. The conductivity of the fluid was equal to 5 S/m, while the conductivity of the matrix was changed $\sigma_M \in [10^{-7}, 10^4]$. We used the stopping criteria that the residual reaches 10^{-8} and ploted the number of iterations for two samples with different contrasts between the fluid and solid conductivity (Fig. 3). According to the presented results, the number of iteration is minimal if the contrast is low and increases with growing contrast.

In the Table (1) we represent the number of iterations, the time per iteration in seconds, and the wall-clock time for simulations with changed values of the matrix conductivity. Please note, that for the models with the size of 400^3, the average iteration time is about 1.22 s and the wall-clock time is proportional to the total number of iterations. However, it does not exceed 500 s for a wide range of conductivity values (Table 1).

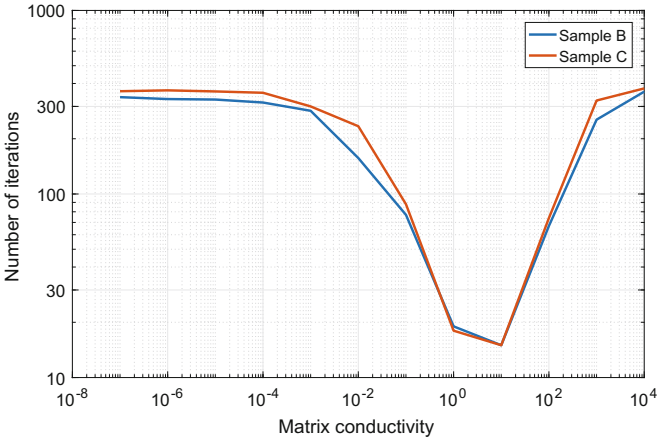

Fig. 3. The number of iterations to achieve residual 10^{-8} for changing conductivity contrasts of Bertheimer sandstone.

5.3 Statistical Models

We applied the algorithm to study the relation between the geometrical characteristics of the pore space and the formation factor. Moreover, we applied matrix reduction algorithm to study the evolution of the parameters. To simulate the interface movement, we use the level-set method [12], assuming that the dissolution rate is 0.1h per time step. We considered 100 steps of the matrix reduction process. The synthetic images were generated using truncated Gaussian field method [15] so that a statistical model is defined by two parameters: the mean porosity and the correlation length. We constructed 16 statistical models, with 100 realizations each, with porosity $\phi = \{0.05, 0.1, 0.15, 0.2\}$ and correlation length $\lambda = \{5, 10, 15, 20\}$ voxels. Thus, in total, we generated 1600 images of 250^3 voxels each. We measured the Minkowski functionals corresponding to the total porosity and specific surface area and also estimated formation factors at each step of matrix reduction process. So, 160000 simulations were done in total. Minkowski functionals for different statistical models averaged over the realizations are presented in Fig. 4. Formation factors are provided in Fig. 5. Note,

Table 1. The number of iterations, the time per iteration and the wall-clock time for the Bentheimer sandstone experiments.

		Sample B			Sample C	
σ_M	N it	Time(s)	T/it.(s)	N it	Time(s)	T/it.(s)
10^{-7}	367	454.44	1.23	363	472.43	1.3
10^{-6}	359	438.78	1.22	367	459.41	1.25
10^{-5}	357	435.28	1.22	362	439.76	1.21
10^{-4}	352	426.87	1.22	356	430.81	1.21
10^{-3}	284	346.05	1.22	300	367.0	1.24
10^{-2}	157	191.32	1.22	234	291.23	1.25
10^{-1}	77	94.58	1.32	88	110.35	1.28
10^{0}	19	25.37	1.33	18	23.08	1.33
10^{1}	15	20.07	1.24	15	20.32	1.23
10^{2}	67	83.41	1.22	74	91.57	1.23
10^{3}	254	310.2	1.21	323	396.26	1.21
10^{4}	361	438.55	1.23	367	457.5	1.24

that formation factor is well-correlated with the sample porosity. Indeed, the initial correlation length of the Gaussian random field affects the rate of the matrix reduction and changes in the specific surface. However, similar porosity values correspond to similar formation factors of the samples, regardless to the correlation length.

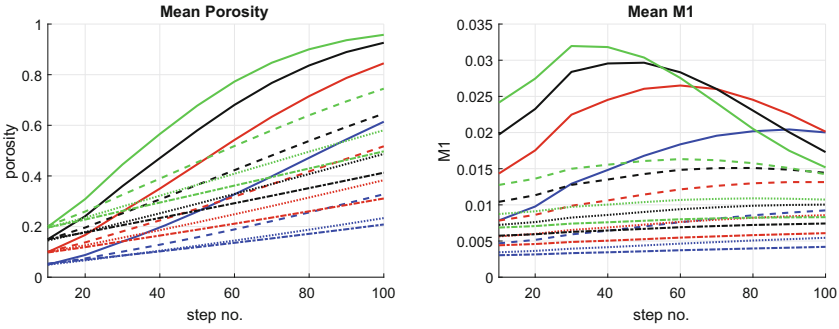

Fig. 4. Porosity and the Minkowski functional 1 for different models. Blue lines correspond to $\phi = 0.05$, red lines correspond to $\phi = 0.1$, black - $\phi = 0.15$, and green - $\phi = 0.2$, solid lines correspond to $\lambda = 5$, dashed - $\lambda = 10$, dotted - $\lambda = 15$, and dasher-dotted - $\lambda = 20$.

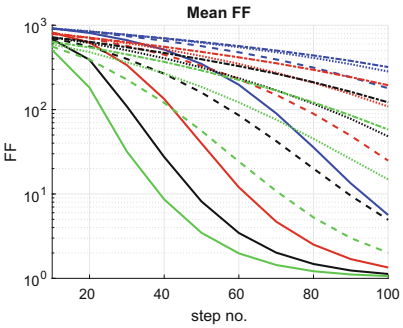

Fig. 5. Formation factors for different models. Blue lines correspond to $\phi = 0.05$, red lines correspond to $\phi = 0.1$, black - $\phi = 0.15$, and green - $\phi = 0.2$, solid lines correspond to $\lambda = 5$, dashed - $\lambda = 10$, dotted - $\lambda = 15$, and dasher-dotted - $\lambda = 20$. (Color figure online)

5.4 Application to Carbonate Rocks

We applied the developed algorithm to estimate the formation factor of the carbonate rock. The model is described in details in [2] and the CT-scans are provided in [1]. In total, four carbonate samples are available.CO_2 was injected into these samples, which resulted in partial dissolution of calcite and erosion of the pore space. On [1], ten micro-CT scans are available for each sample at different time points. The samples were grouped in two pairs depending on the flow rate used in laboratory experiments. Typically, the higher the flow rate, the faster the matrix dissolves and wormholes form. A detailed description of samples and lab experiments are provided in [2]. We use the same designations for the samples: AH and BH correspond to high flow rates, while AL and BL correspond to low flow rate. We performed simulations using subsamples of the size of 400^3 from each sample (the same for all images at different time points). After chemical dissolution of the matrix, it was formed the wide wormholes for the samples where the fluid flow rate was high, which significantly reduces the formation factors. A wormhole was formed in sample AL, where a low fluid flow rate was used due to the preexisting preferred path in the sample, which also resulted in the form-factor decrease. On the contrary, it was observed a weak dissolution in sample BL. Thus there were no changes in form-factor. We provide plots of form-factors for all four experiments as a functions of time, which clearly demonstrate the significant reduction in the rate of changes in pore space during the formation of wormholes (Fig. 6). Please note, that in all cases the iterations number before the convergence of the algorithm varies within 400–1100 iterations and depends on the geometry of the pore space and the complexity of the topology and may require additional study. In contrast, the time per iteration is stable for all experiments.

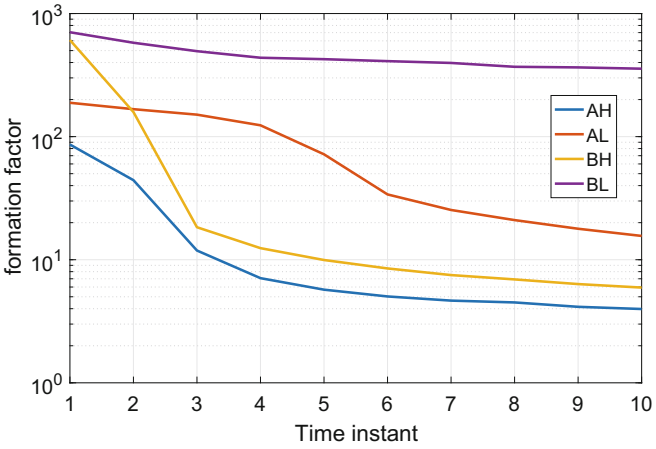

Fig. 6. Pore space of BL carbonate image at the fist (left) and last (right) instant of dissolution.

6 Conclusions

We developed the algorithm for numerical simulation of the potential electric field in porous media. The base of the algorithm is the Krylov-type solver for the discretized Poisson equation. The inverted Laplace operator for homogeneous media is used as a preconditioner, calculated using FFT in the directions, which are normal to the potential change direction. Then we solve a series of one-dimensional problems with using the Thomas algorithm. The solver is implemented on GPU, which allows solving the problems of voxel sizes up to 400^3 with a single GPU. The iterations number is practically independent of the size of the model. However, this depends on the conductivity contrast between the fluid and the rock matrix and the geometrical complexity of the pore space. We applied the algorithm to investigate the evolution of the carbonate samples form-factor during CO_2 sequestration. We have shown that due to the chemical dissolution of the carbonate matrix, the form-factor of the samples increases. However, the rate changes are slowed down when wormholes are formed.

Simulation were performed using computational resources of Peter the Great Saint-Petersburg Polytechnic University Supercomputing Center (www.spbstu.ru).

References

1. Al-Khulaifi, Y., Lin, Q., Blunt, M., Bijeljic, B.: Pore-scale dissolution by CO2 saturated brine in a multi-mineral carbonate at reservoir conditions: impact of physical and chemical heterogeneity (2019). https://doi.org/10.5285/52b08e7f-9fba-40a1-b0b5-dda9a3c83be2

2. Al-Khulaifi, Y., Lin, Q., Blunt, M.J., Bijeljic, B.: Pore-scale dissolution by co2 saturated brine in a multimineral carbonate at reservoir conditions: impact of physical and chemical heterogeneity. Water Resour. Res. **55**(4), 3171–3193 (2019)
3. Alpak, F.O., Riviere, B., Frank, F.: A phase-field method for the direct simulation of two-phase flows in pore-scale media using a non-equilibrium wetting boundary condition. Comput. Geosci. **20**(5), 881–908 (2016)
4. Andra, H., et al.: Digital rock physics benchmarks - part i: imaging and segmentation. Comput. Geosci. **50**, 25–32 (2013)
5. Andra, H., et al.: Digital rock physics benchmarks - part ii: computing effective properties. Comput. Geosci. **50**, 33–43 (2013)
6. Bazaikin, Y., et al.: Effect of CT image size and resolution on the accuracy of rock property estimates. J. Geophys. Res. Solid Earth **122**(5), 3635–3647 (2017)
7. Belonosov, M., Kostin, V., Neklyudov, D., Tcheverda, V.: 3D numerical simulation of elastic waves with a frequency-domain iterative solver. Geophysics **83**(6), T333–T344 (2018)
8. Brown, D.L., Cortez, R., Minion, M.L.: Accurate projection methods for the incompressible Navier-stokes equations. J. Comput. Phys. **168**(2), 464–499 (2001)
9. Chandrasekaran, S., Dewilde, P., Gu, M., Somasunderam, N.: On the numerical rank of the off-diagonal blocks of Schur complements of discretized elliptic PDEs. SIAM J. Matrix Anal., 2261–2290 (2010)
10. Dorn, C., Schneider, M.: Lippmann-Schwinger solvers for the explicit jump discretization for thermal computational homogenization problems. Int. J. Numer. Meth. Eng. **118**(11), 631–653 (2019)
11. Gerke, K.M., Karsanina, M.V., Katsman, R.: Calculation of Tensorial flow properties on pore level: exploring the influence of boundary conditions on the permeability of three-dimensional stochastic reconstructions. Phys. Rev. E **100**(5), 053312 (2019)
12. Gibou, F., Fedkiw, R., Osher, S.: A review of level-set methods and some recent applications. J. Comput. Phys. **353**, 82–109 (2018)
13. Haber, E., Ascher, U.M.: Fast finite volume simulation of 3D electromagnetic problems with highly discontinuous coefficients. SIAM J. Sci. Comput. **22**(6), 1943–1961 (2001)
14. Haber, E., Ascher, U.M., Aruliah, D.A., Oldenburg, D.W.: Fast simulation of 3D electromagnetic problems using potentials. J. Comput. Phys. **163**(1), 150–171 (2000)
15. Hyman, J.D., Winter, C.L.: Stochastic generation of explicit pore structures by thresholding Gaussian random fields. J. Comput. Phys. **277**, 16–31 (2014)
16. Johansen, H., Colella, P.: A cartesian grid embedded boundary method for Poisson's equation on irregular domains. J. Comput. Phys. **147**(1), 60–85 (1998)
17. Kostin, V., Solovyev, S., Bakulin, A., Dmitriev, M.: Direct frequency-domain 3D acoustic solver with intermediate data compression benchmarked against time-domain modeling for full-waveform inversion applications. Geophysics **84**(4), T207–T219 (2019)
18. Lee, B., Min, C.: Optimal preconditioners on solving the Poisson equation with Neumann boundary conditions. J. Comput. Phys. **433**, 110189 (2021)
19. Lisitsa, V., Podgornova, O., Tcheverda, V.: On the interface error analysis for finite difference wave simulation. Comput. Geosci. **14**(4), 769–778 (2010)
20. Lisitsa, V., Bazaikin, Y., Khachkova, T.: Computational topology-based characterization of pore space changes due to chemical dissolution of rocks. Appl. Math. Model. **88**, 21–37 (2020). https://doi.org/10.1016/j.apm.2020.06.037

21. Molins, S., et al.: Pore-scale controls on calcite dissolution rates from flow-through laboratory and numerical experiments. Environ. Sci. Technol. **48**(13), 7453–7460 (2014)
22. Pleshkevich, A., Vishnevskiy, D., Lisitsa, V.: Sixth-order accurate pseudo-spectral method for solving one-way wave equation. Appl. Math. Comput. **359**, 34–51 (2019)
23. Saad, Y.: Iterative Methods for Sparse Linear Systems. SIAM (2003)
24. Samarskii, A.A.: The Theory of Difference Schemes, Pure and Applied Mathematics, vol. 240. CRC Press (2001)
25. Stuben, K.: A review of algebraic multigrid. J. Comput. Appl. Math. **128**(1–2), 281–309 (2001)
26. Vishnevsky, D., Lisitsa, V., Tcheverda, V., Reshetova, G.: Numerical study of the interface errors of finite-difference simulations of seismic waves. Geophysics **79**(4), T219–T232 (2014)
27. Wiegmann, A., Zemitis, A.: EJ-HEAT: a fast explicit jump harmonic averaging solver for the effective heat conductivity of composite materials (2006)
28. Zhan, X., Schwartz, L.M., Toksöz, M.N., Smith, W.C., Morgan, F.D.: Pore-scale modeling of electrical and fluid transport in Berea sandstone. Geophysics **75**(5), F135–F142 (2010)